Rezayee *et al. Geoscience Letters* (2023) 10:43
https://doi.org/10.1186/s40562-023-00298-3

Geoscience Letters

RESEARCH LETTER

Open Access

Structural analysis and susceptibility inversion based on ground magnetic data to map the chromite mineral resources: a case study of the Koh Safi Chromite Ore Deposit, Parwan, Afghanistan

Mohammad Hakim Rezayee[1*], Mahdi Khalaj[2] and Hideki Mizunaga[1]

Abstract

The Koh Safi Chromite Ore Deposit is located in Afghanistan's northern–northeastern end of the Kabul–Kandahar ophiolite zone. Sedimentary formations, delayed volcanic, and ultramafic rock groups, including peridotites and serpentinites, could all have been found in the Koh Safi area, where structural discontinuities with the two trends of northwest–southeast and east–west can be identified. High-grade serpentinite units have many chromite deposits, whereas peridotite has a lot of medium-grade deposits. This paper performs a ground magnetic data analysis based on structural analysis and 3-D susceptibility inversion. The boundaries of structural faults and anomalous bodies are likely delineated in a northwest-to-southeast orientation using a series of derivative maps, including Total Horizontal Derivative, Analytical Signal, and Theta Map. For inversion, many regularization norms that included the range of smooth, intermediate, and compact models were used to examine a particular susceptibility value that occurred in a model cell. The sparse and blocky norms [0,1,1,1] were suggested for our inversion in field data based on synthetic data to determine an appropriate norm. A 3-D inversion of ground magnetic data shows that the highly magnetic zone supposed to be the host rocks seems to be where chromite occurs in the study area.

Keywords Koh Safi, Chromite, Magnetic data, Structural analysis, Inversion

Introduction

Deposits of chromite are a significant source of chromium, the only mineral for chromium widely used in the steel industry (to give steel hardness, toughness, and chemical resistance), in the production of Nichrome (an alloy of iron and nickel used to make high temperature, abrasion, corrosion, and oxidation resistant heating units), and in the plate and paint industries. The primary host rocks for chromite include serpentinite, peridotite, harzburgite, and cumulate dunite (Roberts 1988). Economic deposits can take the shape of stratiform, pod-like tabular lenses, irregular masses, or cumulate layers with various sizes (Mosier et al. 2012). The smaller bodies are found in the highest mantle sequence (harzburgite and dunite), while the larger ones (scattered) are located in, the deeper ultramafic and Gabbro cumulates sequence (Mosier et al. 2012). Podiform chromite bodies are widely distributed in the ultramafic section of ophiolitic formations (Ahmed et al. 2009; Miura et al. 2012; Paktunc 1990; Rollinson 2005). The serpentinization of these ultramafic

*Correspondence:
Mohammad Hakim Rezayee
rezayee.mohammadhakim.624@s.kyushu-u.ac.jp
[1] Department of Earth Resources Engineering, Graduate School of Engineering, Kyushu University, 744 Motooka, Nishi Ward, Fukuoka, Fukuoka, Japan
[2] Kabul, Afghanistan

rocks might be different in degree (Abu El Ela and Farahat 2010; Ahmed 2013; Grieco and Merlini 2012).

Exploring hidden deposits has been difficult despite advances in understanding podiform chromite's origin and fundamental geology (Frasheri 2009). Geophysical techniques have been applied to find orebodies, map geologic structures, and analyze the variables influencing mineralization (Frasheri 2009). Gravity and magnetic methods have been used extensively for chromite prospecting since the 1940s due to variations in orebody density and magnetic susceptibility between an orebody and its host rocks (Davis et al. 1957; Frasheri 2009; Hammer 1945; Sigmund Hammer et al. 1945; Yüngül, 1956). For indirect chromite exploration, a variety of geophysical techniques have been explored, including induced polarization (IP) and magnetotellurics (MT) (He et al. 2018; Xi et al. 2013). Inversion approaches for exploration and applying gravity and magnetic data processing have recently made progress (Batista-Rodríguez et al. 2007; He et al. 2014; Mandal et al. 2013).

Chromite is widely distributed in Afghanistan, particularly in the east and southeast. It occurs in the provinces of Vardak, Logar, Kandahar, Khost, Paktia, Nangarhar, and Kandahar (Abdelaziz et al. 2018). Chromite mineralization was initially identified in the Logar region in 1949–1950 by the United States Bureau of Mines (USBM). This study numbered 1 through 10 outcropping chromite deposits found as huge lenses, pods, and irregularly shaped masses of mostly massive chromite. 18 lenticular chromite masses, some of which had already been recognized by USBM, were discovered via a subsequent investigation by the Federal Institute for Soil Research (Benham et al. 2009).

We aim to improve our knowledge of the 3-D structures and composition of the Koh Safi Chromite Ore Deposit using structural analysis and the inversion approach of the high-resolution ground magnetic data and field samples. Using such better knowledge, we may more clearly characterize the prospective chromite resources in the Koh Safi Chromite Ore Deposit. We used 3-D unconstrained sparse and blocky inversion of the ground magnetic data to reach our objective. Then, we built a 3-D subsurface model using the recovered susceptibility models. At the Koh Safi Chromite Ore Deposit, this model depicts the spatial pattern of the different lithological units.

The rest of this article is divided into the following sections. Before showing the physical properties recovered from geophysical data, we first briefly go through the geology setting, structural analysis, inversion approach, and general impact of different model norms on the model using synthetic data. We describe each section in our result model and compare our proposed exploration targets with existing data, including geological evaluation sections. The final part provides a summary of the general results of this research.

Geology

Afghanistan's regional geology is complicated and diverse due to its location on the tectonic plate boundary. The country's rock age ranges from the Archean to the current era. The Gondwana subcontinent comprises the southern portion of Afghanistan, whereas Eurasia comprises the northern portion (north of the Herat/Badakhshan fault system). Afghanistan is believed to have a fairly complete suite of Archean and Proterozoic rocks, alternated via faulting with all Phanerozoic bedrock systems the overall set overlaps with various Quaternary sediments and structures that increase complexity. Much of the Phanerozoic has an orogenic collage that is very well known, while the Precambrian is less complex (Shroder et al. 2022). As a result, Afghanistan is made up of many distinct crustal blocks, each of which has a unique metallogenic character and is separated from the others by large fault zones (Debon et al. 1987), which range from Afghanistan and West Pakistan to the Arabian Peninsula, are a group of ultramafic–mafic rocks that host chromite deposits in Afghanistan. They were formed during the Eocene.

The Koh Safi Chromite Ore is found in the Kabul–Kandahar ophiolitic zone. These ophiolites are the remains of the ocean crust forced onto the Kabul platform during the Alpine ridge and located in the Tethyan basin. The fault is the primary cause of this drift, located east of this zone—the major faults described above are illustrated in Fig. 1c. Quaternary units have, in certain places, covered ophiolitic units, creating a layer.

In the Koh Safi area, structural discontinuities (mostly faults) trending from the northwest to southeast and east to west are primarily linked to high-grade chromite deposits (Fig. 1a). The slope of the serpentinite units and the chromite lenses within them is also toward the east to northeast, as is the slope of the structural units governing the serpentinites and the main slope of the sedimentary units. Chromite is found in its serpentine host rock as floating particles. In addition, chromite mineralization is intimately connected to dunite shells in harzburgite–dunite regions. Peridotite PR2, PR1, and harzburgite–dunite units are all affected by the circumstances mentioned above Fig. 2. Nevertheless, dunite–chromite occurrences are somewhat diminished in peridotite units.

Our geological investigation suggests two distinct occurrences of chromite mineralization in the study area. It is possible to distinguish between chromites connected to serpentinites and diapirism, and harzburgite–dunite

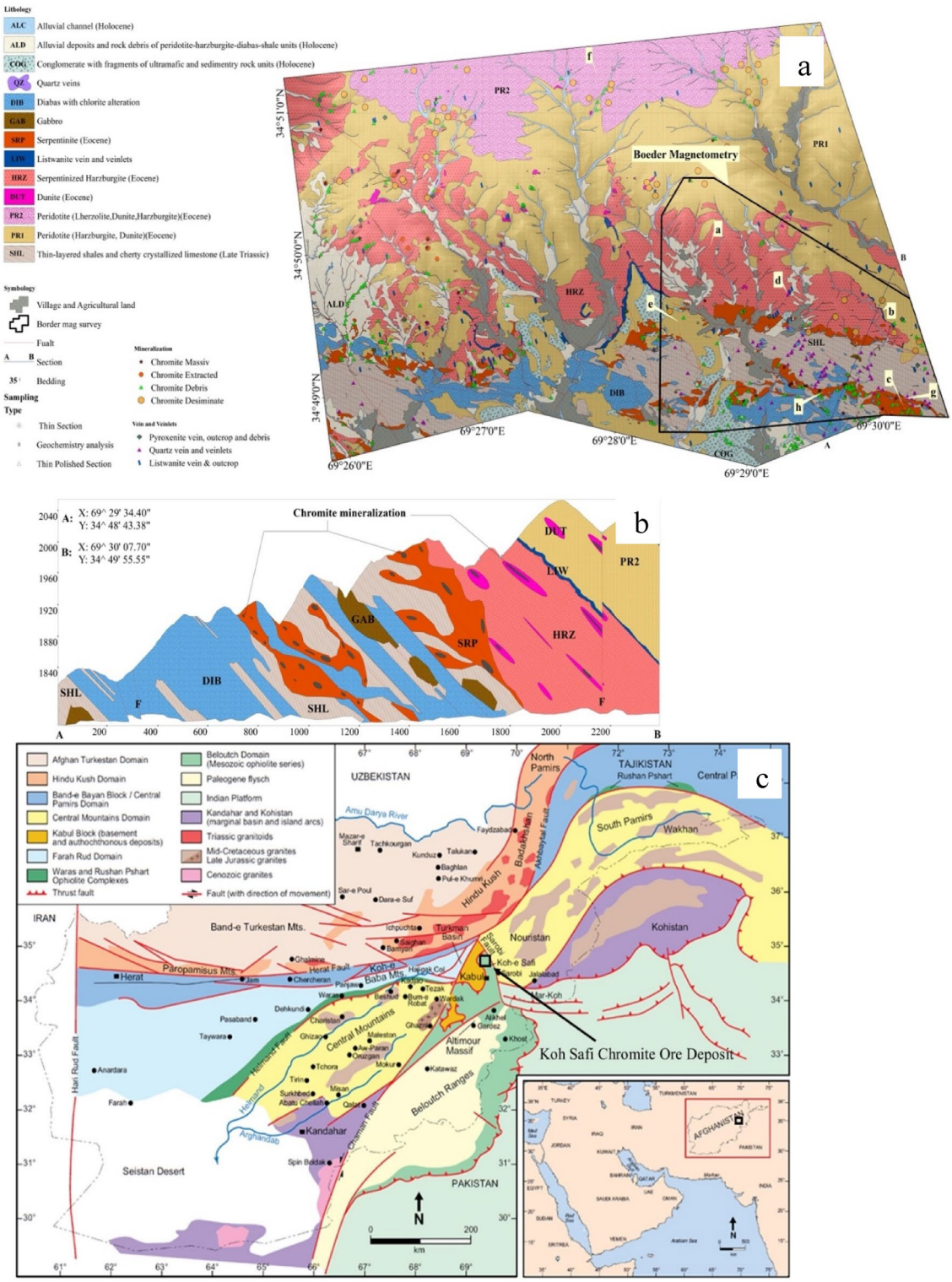

Fig. 1 **a** The geological map of the study area indicates the faults system and lithological composition. **b** The cross-section map along the AB line over the magnetic survey study area illustrates the contact of each unit. **c** Afghanistan's geotectonic system map adapted from (Montenat 2009) illustrates the major structural blocks. Koh Safi area is in the middle of the image

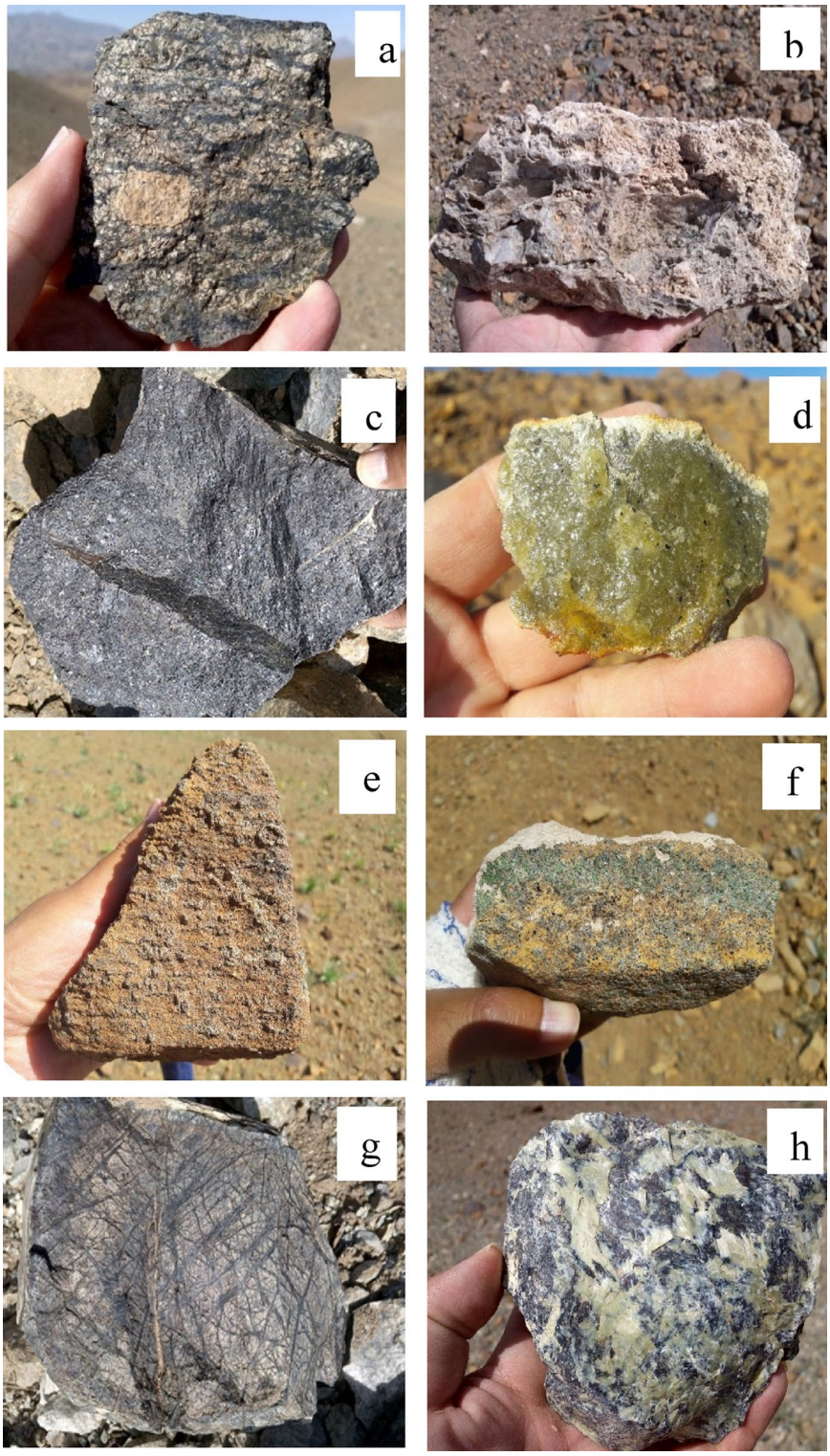

Fig. 2 **a** Harzburgite unit with clear orthopyroxene crystals, **b** Quartz-carbonated veins, **c** High-grade chromite, **d** Dunite with disseminated chromite texture, **e** PR1 peridotites with high OPX values and the compound mainly harzburgite, **f** PR2 peridotite with CPX values much higher than PR1, **g** Serpentinite unit containing multiple veins of magnetite, and **h** Serpentinite with soap gloss. The locations of these collected samples are indicated on the study area's geological map in Fig. 1

units. Serpentines include chromites, but they have split apart, have high grades, and have no spatial relationships, while the chromites associated with the dunites are larger, have a lower grade than the first type and have a more distinct spatial relationship with each other. Because of this, dunite may be used to detect chromite. It means dunites can serve as a crucial discovery key even though type II chromites are typically connected to them. Naturally, it should be noted that not all dunite pods include chromite, but at the stage of supplementary explorations, it may substantially enable the exploration to target. Therefore, the exploration system is different in these two types (Fig. 3). It should be noted that serpentinites exist as small diapers in two bands parallel to each other and on the sides of the sedimentary units, with an approximately east–west trend in the exploration area. Faults generated by a serpentinite diapirism resulted in diabase volcanism.

Magnetic data

A high-resolution ground magnetic survey was conducted throughout multiple campaigns, sampling the total magnetic field along the profiles at intervals of 10 m with the Gem-system GSM-19T Proton Magnetometer. The distance between each line was designed to be 10 m across the magnetic survey area. It boasts an enormous memory storage capacity of 32 Mbytes and a 0.05 nT sensitivity. The diurnal variations were corrected from the total magnetic field values measured at the observatories. A total magnetic anomaly (TMA) map was created after the data were visually reviewed and spikes were manually deleted (Fig. 4a). The International Geomagnetic Reference Field (IGRF) values were then subtracted from the TMA measurements.

Consequently, the north magnetic pole was selected as the reduction point for the gridded TMA values. Consequently, the TMA readings were transformed

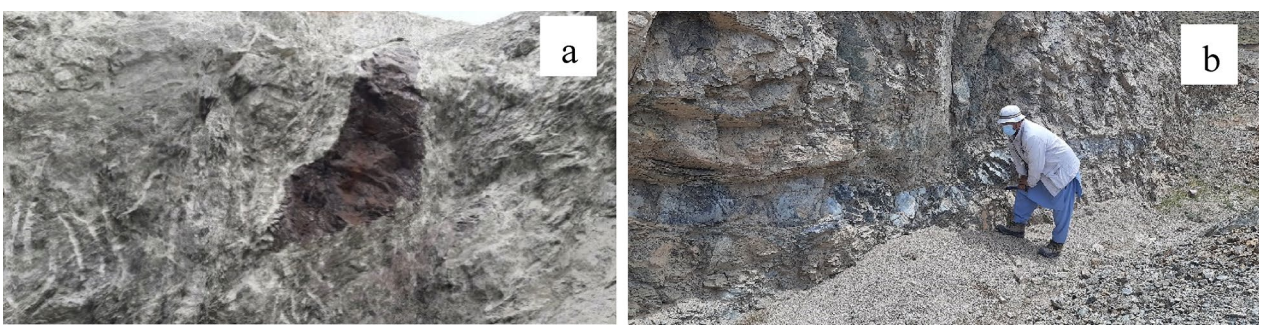

Fig. 3 Serpentinite units with little chromite. **a** The black area in this image is chromite colored, although having a higher grade, and the thickest part's width is less than 2 m. **b** Mineralization of chromite in the Peridotite-bearing dunite pod. In this form of mineralization, expansion and storage volume are larger

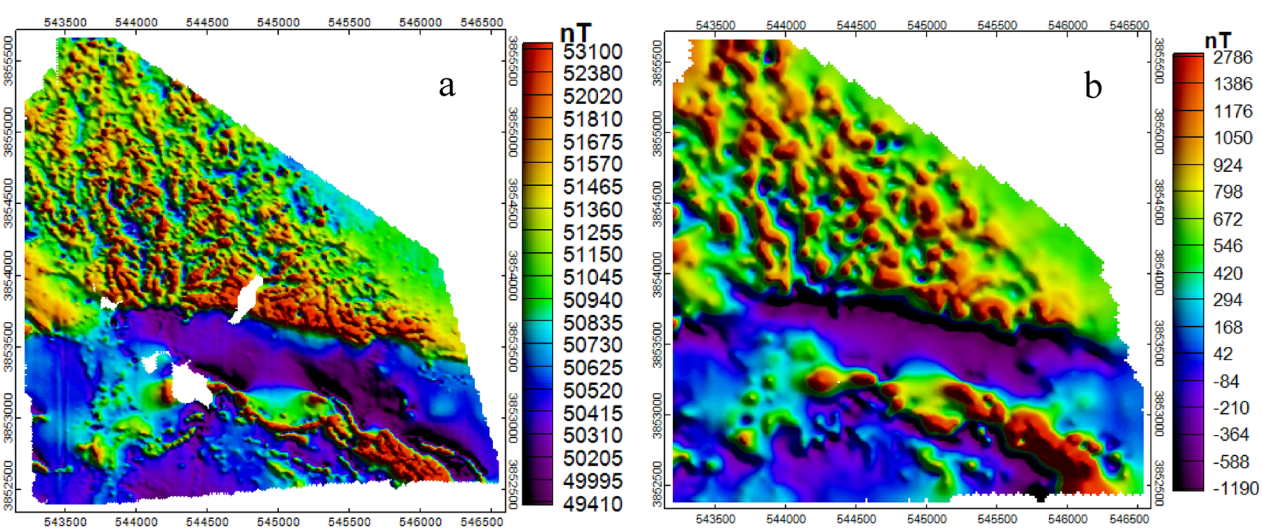

Fig. 4 **a** Total Magnetic Anomaly after diurnal correction, and **b** The total magnetic intensity after diurnal correction, IGRF subtraction, and reduction to pole. The total magnetic intensity refers to the overall strength of the magnetic field at a given point, whereas total magnetic anomaly concentrates on a deviation or fluctuation of the magnetic field from the value expected

to the north magnetic pole after gridding. Values of 54.4° for the inclination and 3.5° for the declination were used to compensate for the distortion caused by the earth's magnetic field's inclination to reposition magnetic anomalies directly over their sources. Significant high magnetic bodies with a high magnetic value of more than 2000 nT are evident in the total magnetic intensity (TMI) reduced to the pole (Fig. 4b), which stretches from the southern parts of the area and trends roughly east to west. The sedimentary composition, which includes shale and limestone associated with negative magnetic anomalies, spread in the northern part of this trend. The serpentinized-harzburgite alternation occurred in a greater area split by alluvial channels in the northern part. These serpentinized-harzburgite occurrences typically correspond with strong positive anomalies that commence in the northern–southern orientation. The fact that the alluvial channel widened as deposits made sedimentary parts on both sides and caused a lower magnetic anomaly is important.

Structural analysis

A series of derivative maps define the boundaries of structural faults and anomalous bodies. We examine the outcomes of three other comparable procedures to assess these solutions' feasibility. They are the total horizontal derivative, analytical signal, and the theta map of the magnetic data. Cooper and Cowan (2011) frequently employed the total horizontal derivative (THD):

$$\mathrm{THD} = \sqrt{\left(\frac{\partial M}{\partial x}\right)^2 + \left(\frac{\partial M}{\partial y}\right)^2}, \tag{1}$$

The THD method's maxima are found around the boundaries of causative sources. We employ a series of profiles of horizontal derivatives of a magnetic anomaly to show the advantages of this approach for strengthening edges in magnetic field data. Analytic Signal (Ma and Li 2012; Roest and Pilkington 1993) of a magnetic intensity anomaly is defined as follows:

$$\boldsymbol{A} = \frac{\partial M}{\partial x}\hat{\mathbf{x}} + \frac{\partial M}{\partial y}\hat{\mathbf{y}} + i\frac{\partial M}{\partial z}\hat{\mathbf{z}}, \tag{2}$$

In Eqs. (1) and (2), M is the magnetic intensity, i is the imaginary unit ($i^2 = -1$, and $\widehat{\mathbf{x}}$, $\widehat{\mathbf{y}}$, and $\widehat{\mathbf{z}}$ are unit vectors in a Cartesian coordinate system. $\partial M/\partial z = 0$ directly over a vertical contact so that the angle between the analytic signal vector and the horizontal θ is $= 0$. The angle is calculated by defining $\widehat{\mathbf{s}}$ as a unit vector along the analytic signal's horizontal direction, as,

$$\cos(\theta) = \frac{\boldsymbol{A}\cdot\hat{\mathbf{s}}}{|\boldsymbol{A}||\hat{\mathbf{s}}|} = \frac{\sqrt{\left(\frac{\partial M}{\partial x}\right)^2 + \left(\frac{\partial M}{\partial y}\right)^2}}{|\boldsymbol{A}|}, \tag{3}$$

Since the magnitudes of the horizontal gradient and analytic signal are compared in Eq. (2), the theta map may also be seen as a normalized horizontal gradient. The indicator of progress introduced by this normalization effectively eliminates amplitude information while highlighting low amplitude characteristics in a way similar to automated gain control.

Magnetic inversion method

We performed an inversion of the ground geophysical data shown in Fig. 4b to arrive at detailed findings about the structure and composition of the rock formation. For the inversion of magnetic data, we applied the standard smoothness-based Tikhonov regularized inversion technique as outlined in (Li and Oldenburg 1996) to perform mathematically by minimizing the following objective function (Sun et al. 2020):

$$\begin{aligned}\varphi(\boldsymbol{m}) = &\left\|\boldsymbol{W}_d\left(\boldsymbol{d}^{\mathrm{obs}} - \boldsymbol{G}\boldsymbol{m}\right)\right\|_2^2 + \beta(\alpha_s\|\boldsymbol{W}_s(\boldsymbol{m}-\boldsymbol{m}_{\mathrm{ref}})\|_2^2 + \alpha_x\|\boldsymbol{W}_x(\boldsymbol{m}-\boldsymbol{m}_{\mathrm{ref}})\|_2^2\\ &+ \alpha_y\|\boldsymbol{W}_y(\boldsymbol{m}-\boldsymbol{m}_{\mathrm{ref}})\|_2^2 + \alpha_z\|\boldsymbol{W}_z(\boldsymbol{m}-\boldsymbol{m}_{\mathrm{ref}})|_2^2\\ &\text{s.t. } \boldsymbol{m}_{\min} \le \boldsymbol{m} \le \boldsymbol{m}_{\max},\end{aligned} \tag{4}$$

or

$$\varphi(\boldsymbol{m}) = \varphi_d(\boldsymbol{m}) + \beta\varphi_m(\boldsymbol{m}), \tag{5}$$

where $\boldsymbol{m}$ is the model of the recovered physical property; The values of the recovered physical property are constrained by $\boldsymbol{m}_{\min}$ and $\boldsymbol{m}_{\max}$, respectively; $\boldsymbol{W}_d$ is a data weighting matrix made up of data correlations and data uncertainties; $\boldsymbol{d}^{\mathrm{obs}}$ stands for inverted geophysical measurements; $\boldsymbol{G}$ is a symbol for the forward modeling operator, which bridges a model of a physical property to the appropriate geophysical responses; There are discretized spatial weighting matrices denoted $\boldsymbol{W}_i (i = s, x, y, \text{and } z)$;

and a reference model known as $\boldsymbol{m}_{\text{ref}}$ allows consolidation of any prior understanding or geological assumptions. We adopt a zero reference, or $\boldsymbol{m}_{\text{ref}} = 0.0001$, in our investigation and assume no prior information. To account for the probable field data decay with distance (Li and Oldenburg 1996, 1998), we additionally include the sensitivity-based spatial weighting (Li and Oldenburg 2000) into $\boldsymbol{W}_i (i = s, x, y, \text{and } z)$ matrices.

In the literature, the parameter β is commonly called the regularization parameter. It determines the final recovered model's structural complexity and the degree of fitting between observed and predicted data. Although a small β provides a model that closely matches the data, it may also have too much structure, which leads to a large model norm, $\varphi_m(\boldsymbol{m})$ (Trevino et al. 2021). In contrast, if it is high, the optimization leads to a model with less structure and a higher degree of data misfit, $\varphi_d(\boldsymbol{m})$. Due to the nonlinear aspect of the optimization, a gradient-based Gauss–Newton approach is employed. This process is continued until the algorithm converges to a minimum and the misfit threshold is satisfied.

Using the SimPEG inversion framework (Cockett et al. 2015), a mixed $\updownarrow_p$ norm inversion approach was used to invert the magnetic data from 1070 of the 23,394 stations for 3-D susceptibility distribution. With this approach, the objective is to find a single model that exhibits the highest level of smoothness in each of the three spatial directions and can properly reflect the geophysical observations. Using the $\updownarrow_p$ norm where $0 \leq p \leq 2$, regularizations may be adjusted to build smooth or sparse models based on the interpreter's prior knowledge. We employed the approach described (Fournier and Oldenburg 2019), in which Scaled Iteratively Re-Weighted Least Squares (S-IRLS) introduce the sparsity assumptions. Four variables make up our regularization norm, which reflects the susceptibility and the three directional gradients.

Synthetic model

Synthetic data provide controlled settings for analyzing regularization impacts, examining various scenarios and parameter settings, and highlighting patterns and mechanisms in norm regularization, directing future studies in this field. We created a synthetic model of a magnetized dipping sphere (0.1 SI), a magnetized slope dike (0.06 SI), and a magnetized vertical block (0.02 SI) buried in a nonmagnetic background to evaluate the effect of different model norms on the inversion results. We tested all possible $\updownarrow_p$ combinations to accomplish several regularizations rather than just one (Trevino et al. 2021). Nine possible models with the norms [0,0,0,0], [0,1,1,1], [0,2,2,2], [1,0,0,0], [1,1,1,1], [1,2,2,2], [2,0,0,0], [2,1,1,1], [2,2,2,2] are produced by maintaining the equality of the three gradient terms while changing the amplitude term. According to the regularization [0,1,1,1], the susceptibility value has a 0 norm, while the three directional susceptibility gradients have a 1 norm. To retrieve the original model using the nine-regularization norm combinations, we first calculate the magnetic response of this model in the present-day field.

We performed the inversion using a variety of regularization norms that included the scope of smooth, intermediate, and compact models to estimate the probability that a particular susceptibility value appears in a model cell (Fig. 5). We gained the value of a susceptibility arising in each cell using the 9 models. We employed this information as an indicator of our model's robustness. In addition, the apparent susceptibility of certain models tends to underestimate the real susceptibility of the synthetic model, while that of other models tends to overestimate it. No one particular model regularization fully recovers all the real model properties. It should be noted that all models fit the data within the errors.

The smoother norms ($p_s = 2$, Fig. 5a–c) inappropriately exaggerate background susceptibility in comparison to the true model. Though mostly recovered, the block, sphere, and dike have been spread out laterally and vertically. The right-hand expansion of the dike is significantly overestimated, and the top surface of the dike is recovered a few model cells deeper than it is. The intermediate norm better defines the block, sphere, and dike, l_1 models (Fig. 5f–h) and have a reduced background susceptibility. Five or six cells on each side of the block, sphere, and dike underestimate overall thickness.

It is important to highlight that recovered susceptibility for magnetic bodies is overestimated compared to true susceptibility. The compact, l_0 norm models recover the background effectively, while the models with $p_{x,y,\text{ and } z} = (0 \text{ and } 2)$ poorly interpret the block and dike Fig. 6d–f. The sphere is best recovered with norms ($p_{x,y,\text{ and } z} = 1$); however, the block and dike have spread outward from the center.

Model setup

We used the sparse and blocky norms ($p_s = 0, p_{x,y,\text{ and } z} = 1$) for our inversion in field data. The top surfaces and lateral extent of features are often fully recovered, but they may be several cell widths thicker than the true model, which has implications for interpreting our inversion model. The recovered apparent susceptibilities are typically 1 to 2 times higher than the true model, which is significant for interpreting altered zones. These implications indicate that the largest volumes are most likely in the areas of alteration that are interpreted as low apparent susceptibility.

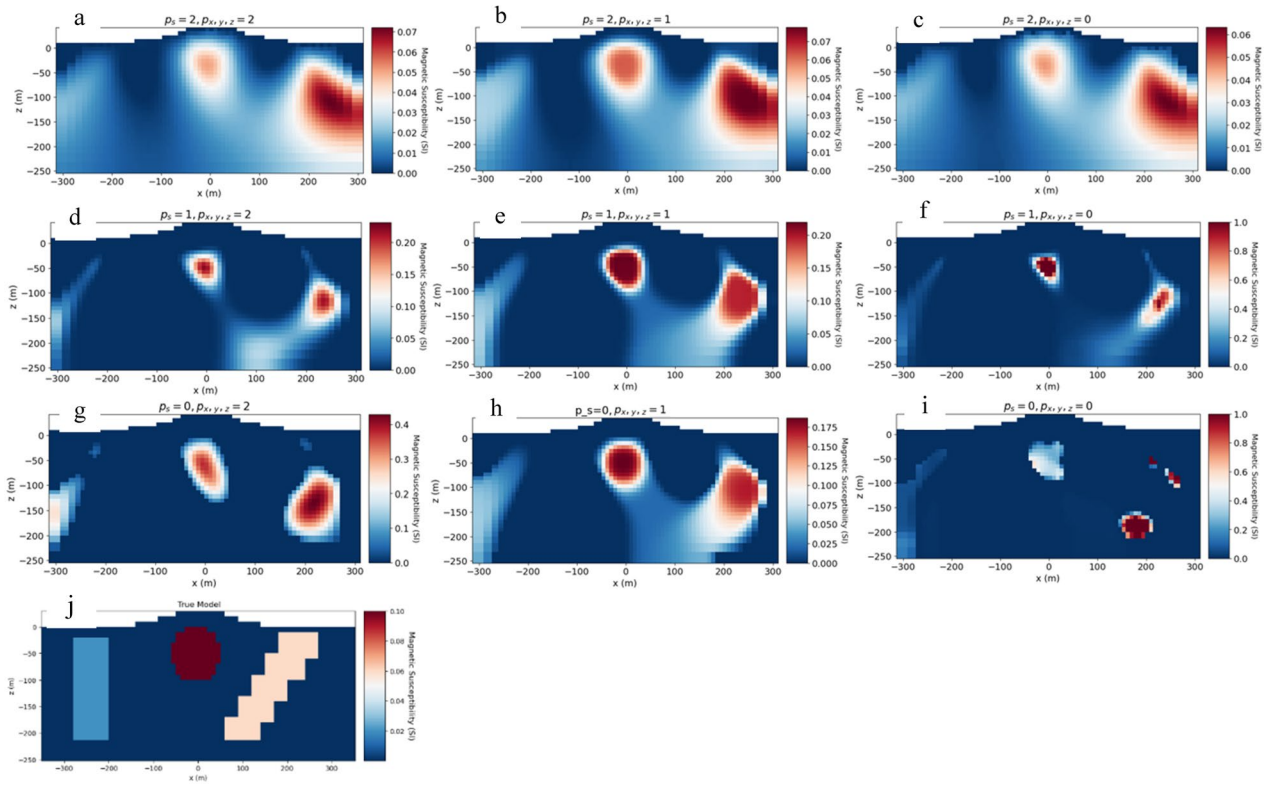

Fig. 5 The effect of various model norms on the model from a synthetic given dataset. Norms with a smooth amplitude constraint, represented by [2,2,2,2], [2,1,1,1], and [2,0,0,0], are shown in the top row (**a**–**c**). Models with a moderate amplitude constraint, such as [1,2,2,2], [1,1,1], and [1,0,0,0], are displayed in the middle row (**d**–**f**). And the models [0,2,2,2], [0,1,1,1], and [0,0,0,0] are displayed in the bottom row (**g**–**i**) of models with a compact amplitude constraint. The true model is illustrated in panel (**j**)

As a target misfit of the number of data points, we used a standard error (σ), 10 nT and 2% of the data range, and chi-factor = 1. After 65 iterations, magnetic inversion reached this floor and converged to a stable model norm, φ_m. The unitless normalized residual [(observed data-calculated data)/(standard error)] inversion with norm [0, 1, 1, 1] is shown in Fig. 7c.

Result and discussion

The structure-enhanced maps displayed the positions and directions of the subsurface structures. The contact locations are shown on the total horizontal derivative (THD) map (Fig. 6a) as maximal amplitude anomalies with values ranging from −0.05 to 0.250 nT/m (normalized). The locations of the detected contacts are shown on the map by the anomaly maxima, which are shown as high values. Considering that these lineaments are generally orientated NW–SE, it can be seen that the study area's southern and northern halves are where the majority of the structures are located, whereas the northern portion is sparsely populated with structures. The findings obtained by THD were accredited using AS based on amplitude peaks over magnetic source boundaries. The AS maxima of the magnetic data offer a clear resolution for the shallow objects, but they do not delineate deeper bodies (Arisoy and Dikmen 2013). The assumption of thick sources in the AS maps yields minimal depth estimations, much like the horizontal gradient approach. Because it calls for the computation of the vertical derivative, the analytical signal approach is more sensitive to noise than the horizontal gradient method. Since the amplitude of the analytic signal is always positive, it may be used to pinpoint the place of the contrast but not its direction. It is determined that the RTP magnetic data's analytical signal is displayed in Fig. 6b.

Peaks of the analytical signal correspond with the main faults' locations in the study area ranging from the northwest to the southeast. On the THD and AS maps, several other important magnetic susceptibility connections and faults can be seen, some of which are main faults' branches. The THD and AS map also displays many magnetic intrusive bodies. Maximum above the contact on a theta map, surrounded by minima on either side Fig. 6c. The theta map is typically challenging to understand alone since it identifies all edges despite eradicating the original TMI amplitudes.

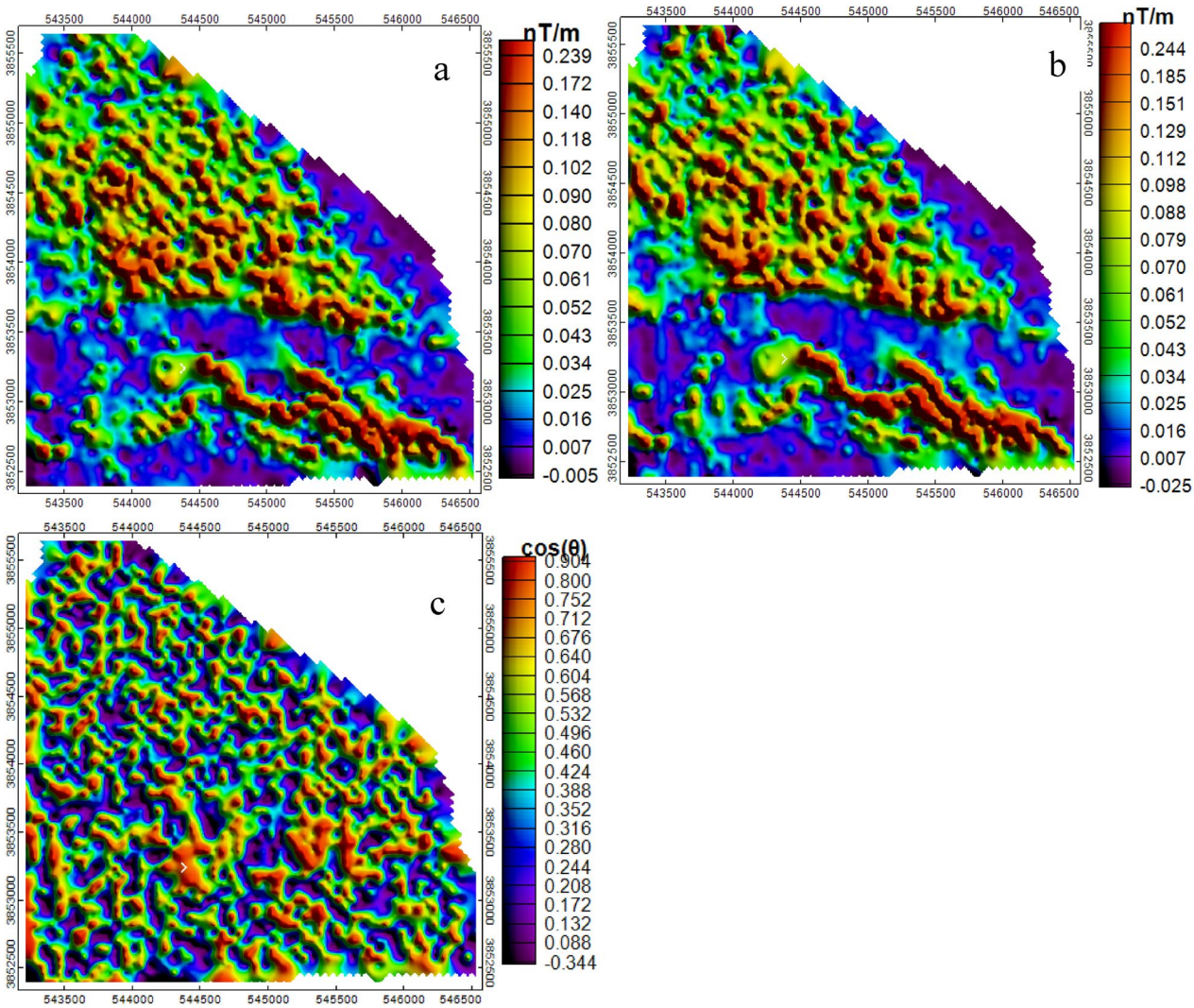

Fig. 6 **a** Total horizontal derivative map, **b** The analytical signal map, and **c** the theta map

The recovered susceptibility model reveals distinct rock compositions based on magnetic susceptibility. Table 1 displays typical susceptibility values for various rock types, highlighting their magnetic properties (Hunt et al. 1995). Horizontal and vertical slices show the inversion results at different depths Fig. 8. We have chosen the free air susceptibility value above the ground (−0.1) to distinguish the ground magnetic features below the surface. The lowest elevation is supposed to be zero meters in topography during the inversion procedure. Figure 8a illustrates the horizontal and vertical slices ($x = 543{,}500$, $y = 3{,}852{,}700$, and $z = 150$), which the horizontal one dominantly covers the central to the northern part of the study area. As displayed on the left upper panel in Fig. 8a, in-depth ($z = 150$) attributed with higher susceptibilities correspond to a close relationship between the surface geological formation and deeper magnetic bodies. The strong predominant component is the serpentinized harzburgite that predominately coexists with this slice's harzburgite and dunite lenses. In the northern area, dunite rock may also be explored as a potential host rock for chromite. Identifying the dunite rock unit in the harzburgite is the major part of this section. Northwest–Southest oriented complexes are signified with high magnetic susceptibility contrast attribution. These magnetic bodies, complicated by local faults and alluvial deposits, visualize the serpentinized-harzburgite alternations. Based on the variation in ultramafic material contents, some central sections comprise peridotite units with high to intermediate magnetic susceptibility. The cross-section in ($y = 3{,}852{,}700$) associated with the lower panel (Fig. 8a) shows the vertical expansion of magnetic bodies, while surface susceptibility is not illustrated on the horizontal slice. This cross-section shows that separate masses

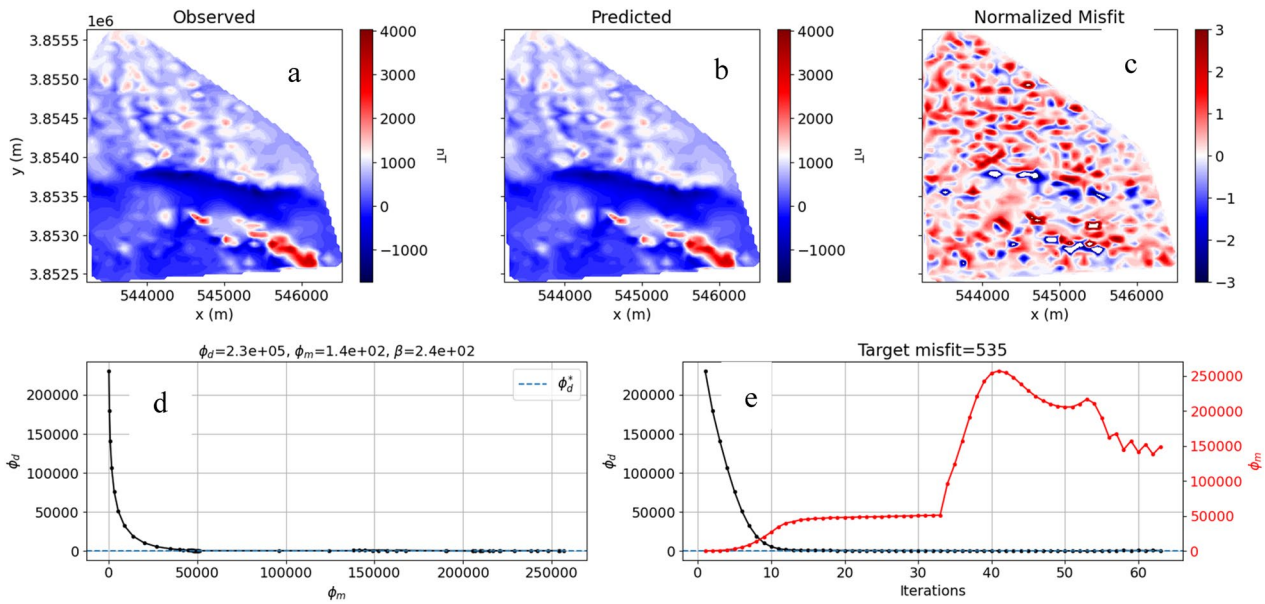

Fig. 7 **a** Observed data. **b** Calculated data for model norm [0,1,1,1]. **c** Spatial distribution of the normalized residual. **d** Tikhonov curve. **e** Convergence curves for the model norm [0,1,1,1] with model norm (φ_m) in red and misfit (φ_d) in black

are located in a low-susceptibility environment and are consistent with the magnetic structure of the southern portion of the study area. These injectable compounds, which have an East–West inclination, are associated with chlorite diabase. Slice at ($x = 543{,}500$) in the upper right panel in Fig. 8 (a) manifests the magnetic susceptibility alteration along the northing direction.

In Fig. 8b, the magnetic structure is displayed in ($x = 544{,}200$, $y = 3{,}853{,}500$, and $z = -200$) which the horizontal slice encases the whole ground in the study area. Based on the magnetic susceptibility model, the dispersed bodies aggregated at a depth of about −200 m. An integrated susceptibility trend is elongated in an eastern-western direction corresponding to the high magnetic susceptibility. This trend is associated with serpentinite composition on the surface. Beyond the southern side, this serpentinite formation is associated with diabase units. In addition, the chromite lens that was so distinctively hosted by this serpentinite was related to softer morphological characteristics from neighboring sections. On the northern side of this serpentinite trend, a deeper valley is apparent with low magnetic susceptibility consisting of sedimentary rocks, including Shale and Limestone. Vertical slices (lower left and upper right in Fig. 8b) indicate the depth of this rerpentintes. On the northern part of this depth, the serpentinized-harzburgite composition is spread with high susceptibility. These serpentinized-harzburgite formations involved a broad area with more depths. It is confirmed via vertical slice in the northing direction in $x = 544{,}200$.

Figure 8c identifies a deeper structure ($z = -500$) related to higher magnetic susceptibility contrast. At this depth, the random spread of magnetic masses disappeared, exposing only larger magnetic objects. The depth of these magnetic bodies is visualized in vertical sections ($x = 545{,}200$, $y = 3{,}854{,}300$) along the east and north directions in Fig. 8c upper right and lower left panels, respectively. Figure 8d exhibits a wide none magnetic area attributed to very low susceptibility contrast. A higher magnetic system surrounds this low susceptible environment. A three-dimensional perspective of the

Table 1 The typical rocks/minerals magnetic susceptibility value adapted from Hunt et al. (1995)

No	Mineral/rocks	Chemical formula	Susceptibility (10^{-6} SI)
1	Diabase		1000–160,000
2	Diorite		630–130,000
3	Gabbro		1000–90,000
4	Peridotite		96,000–200,000
5	Limestone		2–25,000
6	Shale		63–18,600
7	Sandstone		0–20,900
8	Serpentine		3100–18,000
9	Quartz	SiO_2	−13–17
10	Chromite	$FeCr_2O_4$	3000–120,000
11	Serpentinite	$Mg_3Si_2O_5(OH)_4$	31,000–75,000

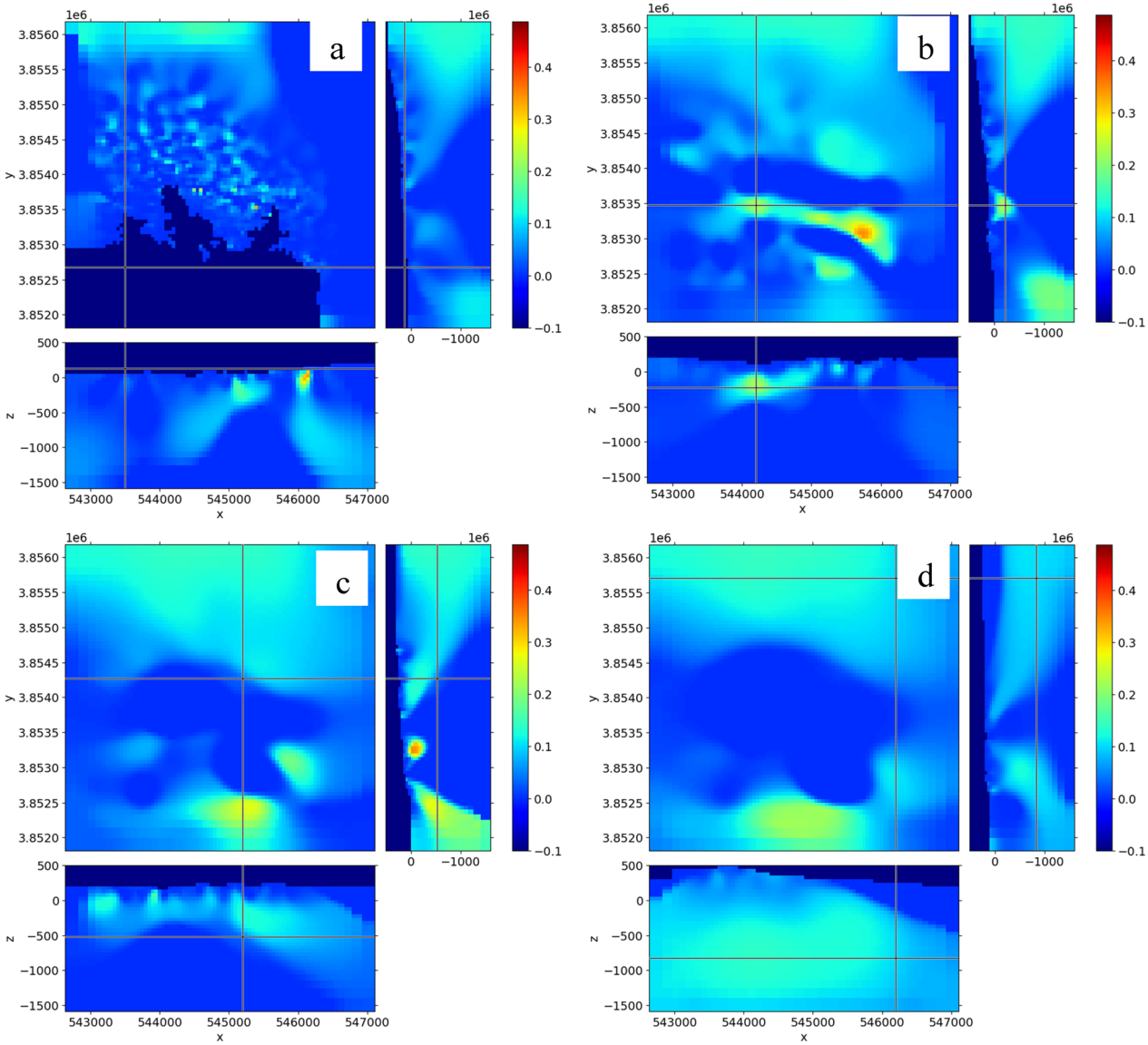

Fig. 8 Plan and sectional views of the three-dimensional recovered model, **a** slices in ($x = 544{,}200$, $y = 3{,}853{,}500$, and $z = 150$), **b** ($x = 543{,}500$, $y = 3{,}852{,}700$, and $z = -200$), **c** ($x = 545{,}200$, $y = 3{,}854{,}300$, and $z = -500$), and **d** ($x = 546{,}200$, $y = 3{,}855{,}400$, and $z = -800$). The vetical and horizontal cross sections in different panels are indicated by gray lines along x, y, and z directions

model with an isosurface of apparent susceptibility > 0.05 SI is illustrated in Fig. 9. This represents the bodies with high magnetic susceptibility associated with chromite mineral occurrence. The geological and TMI maps have been placed over the recovered model's three-dimensional image to understand better rock structure, magnetic anomalies, and apparent susceptibility values.

The relationship between chromite and serpentinite has been thoroughly investigated in the study area. It can be useful to characterize the prospective expansion of chromite ore deposits by mapping the distribution of dunite and serpentinite. Serpentinite and dunite are two ultramafic rocks that frequently contain chromite in the study area. Although chromite has a lower magnetic susceptibility than serpentinite, this is not the only factor in detecting chromite deposits. Instead, attention is paid to identifying the host rocks typically associated with chromite mineralization. We can locate areas where the geological conditions encourage the occurrence of chromite deposits by investigating the extent of dunite and serpentinite based on higher apparent magnetic susceptibility. The possible existence of chromite ore deposits

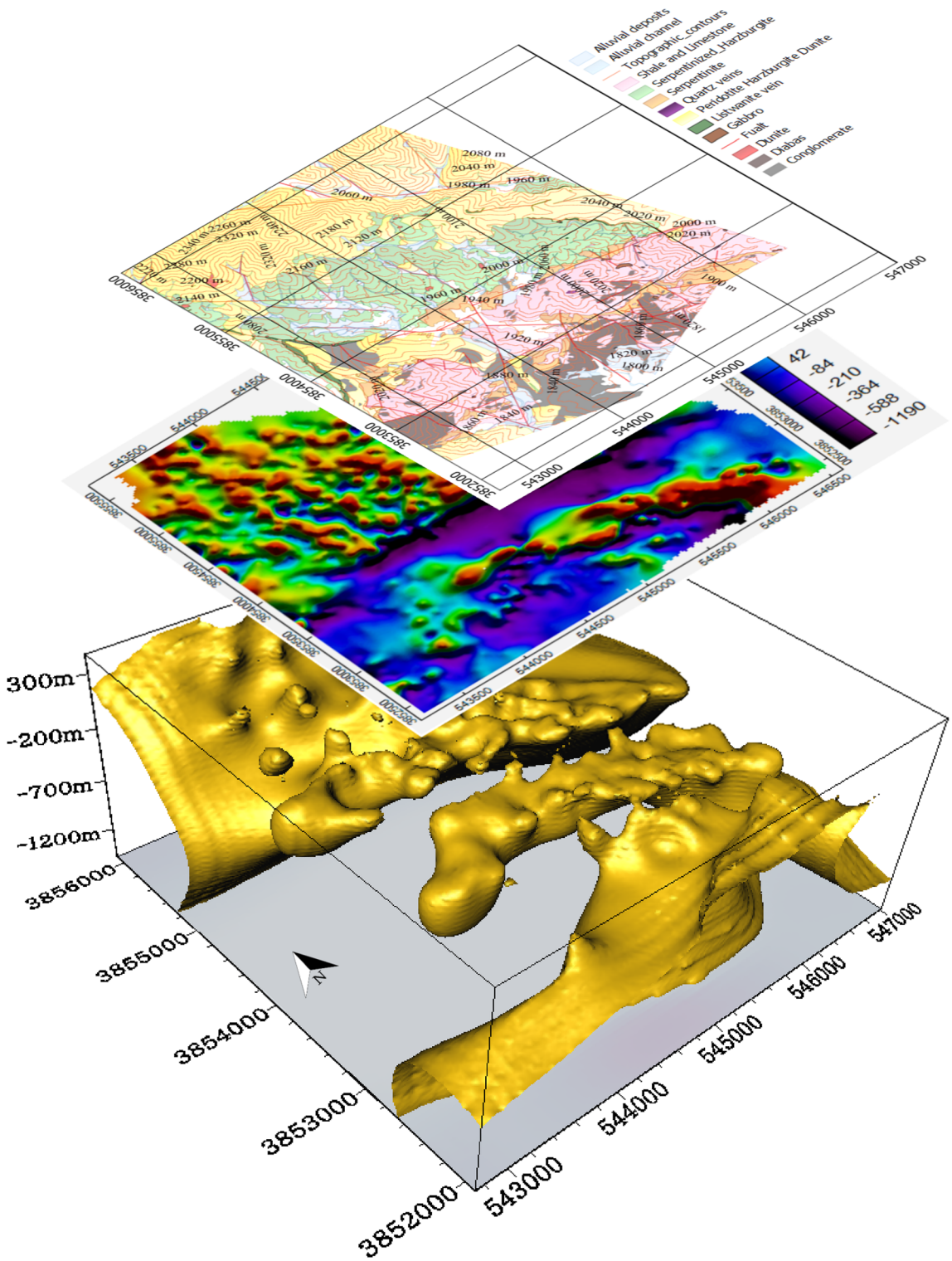

Fig. 9 Three-dimensional representation of the inverse model showing isosurfaces of > 0.05 SI. The geological and TMI maps are overlapped on a three-dimensional view of the recovered model to understand better rock formation, magnetic anomalies, and apparent susceptibility values

can be inferred indirectly from the dunite and serpentinite extension mapping. Because dunite and serpentinite are strongly connected to the mantle and associated with processes like ophiolite formation or mantle upwelling, their presence is interpreted as a geological setting favorable for chromite growth. We can locate regions where chromite-bearing zones are more likely to be discovered by mapping the extent of these rocks.

Conclusion

In this case study, we explored the Koh Safi area's chromite ore deposit circumstances using ground magnetic data. Greater chromite deposits are generally associated with serpentinite rock units, structural discontinuity (often a fault), and an east–west trend in the Koh Safi area. In its serpentine host rock, chromite can be found as floating particles. Chromite mineralization is also closely related to dunite shells in harzburgite–dunite zones. We used derivative methods based on Total Horizontal Derivative, Analytical Signal, and Theta Map to show the overall structure resulting from geological operations. We developed a three-dimensional model by incorporating ground magnetic data to understand better the composition and structures of the Koh Safi Chromite Ore Deposit and the distribution of chromite mineral resources.

We created numerous models with various regularization norms to estimate the uncertainty of our models, statistically examined the variations, and produced different models of apparent susceptibility occurrence using an open-source inversion algorithm (Cockett et al. 2015). As synthetic models guide, we propose recovering features within a sparse and blocky model, favorable within one to four cell widths. Considering many norm models tested on synthetic data, the sparse and blocky norm applied to field data with standard error (σ), 10 nT plus 2% of the data range, and chi-factor = 1.

The relationship between chromite and serpentinite is investigated in the study area. It is possible to find mineralization zones with serpentinite alteration in the study area because chromite mineralization does not occur in massive quantities. Some magnetite is produced during the serpentinization process, and magnetometry can easily identify it. Although chromite has a lower magnetic susceptibility than serpentinite, this is not the only approach to finding chromite deposits. Mapping the distribution of dunite and serpentinite can characterize the expansion of chromite ore deposits. The distribution of highly susceptible units, common host rocks for chromite occurrences in the shallow depth with a maximum depth of more than -500 m, is efficiently recovered by the 3-D magnetic inversion result. As a result of the greater than 0.04 magnetic susceptibility related to serpentinite composition at a depth of −600 m below the surface, an integrated susceptibility trend is extended in the southern region in an east–west direction. This serpentinite formation changes to diabase units beyond the southern edge. Higher susceptibilities for serpentinized-harzburgite composition are associated with greater magnetic anomalies in the northern part of the study area. The main strong component in this section is the harzburgite that has been serpentinized, which is mostly present with the harzburgite and dunite lenses. Outside the northern region, dunite rock could be investigated as a possible host rock for chromite.

Acknowledgements
The authors thank the Hewad Brothers Mining Company (HBMC) for providing the geological and geophysical data. The Project for the Promotion and Improvement of the Afghan Capacity for Effective Development (PEACE), JICA, Japan, is funding the first author.

Author contributions
MHR and MK worked on the conceptualization, methodology, software, data collection, writing and preparation of the original draft, visualization, and research. The supervision, supervision, conceptualization, methodology, investigation, writing, reviewing, and editing were all the responsibilities of HM. The authors read and approved the final manuscript.

Funding
This paper does not build directly on a contemporary grant.

Availability of data and materials
The corresponding author can provide the data sets used and analyzed during this study upon reasonable request.

Declarations

Competing interests
The authors state that they do not have any competing interests.

Received: 16 May 2023 Accepted: 11 September 2023
Published online: 22 September 2023

References

Abdelaziz R, Abd El-Rahman Y, Wilhelm S (2018) Landsat-8 data for chromite prospecting in the Logar Massif,Afghanistan. Heliyon. https://doi.org/10.1016/j.heliyon.2018.e00542

Abu El Ela FF, Farahat ES (2010) Neoproterozoic podiform chromitites in serpentinites of the Abu Meriewa-Hagar Dungash district, Eastern Desert, Egypt: Geotectonic implications and metamorphism. Island Arc. https://doi.org/10.1111/j.1440-1738.2009.00689.x

Ahmed AH (2013) Highly depleted harzburgite-dunite-chromitite complexes from the Neoproterozoic ophiolite, south Eastern Desert, Egypt: a possible recycled upper mantle lithosphere. Precambrian Res. https://doi.org/10.1016/j.precamres.2013.05.001

Ahmed AH, Arai S, Abdel-Aziz YM, Ikenne M, Rahimi A (2009) Platinum-group elements distribution and spinel composition in podiform chromitites and associated rocks from the upper mantle section of the Neoproterozoic Bou Azzer ophiolite, Anti-Atlas, Morocco. J Afr Earth Sci. https://doi.org/10.1016/j.jafrearsci.2009.02.005

Arisoy MÖ, Dikmen Ü (2013) Edge detection of magnetic sources using enhanced total horizontal derivative of the tilt Angle Geliştirilmiş Eğim Açısı Toplam Yatay Türevi ile Manyetik Kaynakların Sınırlarının Belirlenmesi. Bull Earth Sci Appl Res Centre Hacettepe Univ 34(1):73–82
Batista-Rodríguez JA, Pérez-Flores MA, Quiroga-Goode G, Gallardo LA (2007) Geometry of ophiolites in eastern Cuba from 3D inversion of aeromagnetic data, constrained by surface geology. Geophysics. https://doi.org/10.1190/1.2712425
Benham AJ, Kováč P, Petterson MG, Rojkovic I, Styles MT, Gunn AG, Mckervey JA, Wasy A (2009) Chromite and PGE in the logar ophiolite complex, Afghanistan. Trans Inst Min Metal Sect B Appl Earth Sci. https://doi.org/10.1179/174327509X434957
Cockett R, Kang S, Heagy LJ, Pidlisecky A, Oldenburg DW (2015) SimPEG: An open source framework for simulation and gradient based parameter estimation in geophysical applications. Comput Geosci. https://doi.org/10.1016/j.cageo.2015.09.015
Cooper GRJ, Cowan DR (2011) A generalized derivative operator for potential field data. Geophys Prospect. https://doi.org/10.1111/j.1365-2478.2010.00901.x
Davis WE, Jackson WH, Richter DH (1957) Gravity prospecting for chromite deposits in Camaguey Province, Cuba. Geophysics. https://doi.org/10.1190/1.1438427
Debon F, Afzali H, Le Fort P, Sonet J (1987) Major intrusive stages in Afghanistan: typology, age and geodynamic setting. Geol Rundsch. https://doi.org/10.1007/BF01820586
Fournier D, Oldenburg DW (2019) Inversion using spatially variable mixed ℓp norms. Geophys J Int. https://doi.org/10.1093/gji/ggz156
Frasheri AI (2009) The peculiarities of geophysical methods in exploration for chrome deposits. SEG technical program expanded abstracts. 28(1). https://doi.org/10.1190/1.3255091
Grieco G, Merlini A (2012) Chromite alteration processes within Vourinos ophiolite. Int J Earth Sci. https://doi.org/10.1007/s00531-011-0693-8
Hammer S (1945) Estimating ore masses in gravity prospecting. Geophysics. https://doi.org/10.1190/1.1437147
He L, Hu X, Zha Y, Xu L, Wang Y (2014) Distribution and origin of high magnetic anomalies at Luobusa Ophiolite in Southern Tibet. Chin Sci Bull. https://doi.org/10.1007/s11434-014-0330-6
He L, Chen L, Dorji HZ, Wang X, Xiao B, Xu L, Zhao X, Xi X, Yao H, Chen R (2018) Mapping chromite deposits with audio magnetotellurics in the Luobusa ophiolite of southern Tibet. Geophysics. https://doi.org/10.1190/geo2017-0110.1
Hunt CP, Moskowitz BM, Banerjee SK (1995) Magnetic properties of rocks and minerals: a handbook of physical constants. Rock physics and phase relations, vol 3. American Geophysical Union
Li Y, Oldenburg DW (1996) 3-D inversion of magnetic data. Geophysics. https://doi.org/10.1190/1.1443968
Li Y, Oldenburg DW (1998) 3-D inversion of gravity data. Geophysics. https://doi.org/10.1190/1.1444302
Li Y, Oldenburg DW (2000) Joint inversion of surface and three-component borehole magnetic data. Geophysics. https://doi.org/10.1190/1.1444749
Ma G, Li L (2012) Edge detection in potential fields with the normalized total horizontal derivative. Comput Geosci. https://doi.org/10.1016/j.cageo.2011.08.016
Mandal A, Mohanty WK, Sharma SP (2013) 3D compact inverse modeling of gravity data for chromite exploration—a case study from Tangarparha, Odisha, India. Society of exploration geophysicists international exposition and 83rd annual meeting, SEG 2013: expanding geophysical frontiers. https://doi.org/10.1190/segam2013-0898.1
Miura M, Arai S, Ahmed AH, Mizukami T, Okuno M, Yamamoto S (2012) Podiform chromitite classification revisited: a comparison of discordant and concordant chromitite pods from Wadi Hilti, northern Oman ophiolite. J Asian Earth Sci. https://doi.org/10.1016/j.jseaes.2012.05.008
Montenat C (2009) The Mesozoic of Afghanistan. GeoArabia. https://doi.org/10.2113/geoarabia1401147
Mosier DL, Singer DA, Moring BC, Galloway JP (2012) Podiform chromite deposits—database and grade and tonnage models. US Geological Survey Scientific Investigations, Report
Paktunc AD (1990) Origin of podiform chromite deposits by multistage melting, melt segregation and magma mixing in the upper mantle. Ore Geol Rev. https://doi.org/10.1016/0169-1368(90)90011-B
Roberts S (1988) Ophiolitic chromitite formation: a marginal basin phenomenon? Econ Geol. https://doi.org/10.2113/gsecongeo.83.5.1034
Roest WR, Pilkington M (1993) Identifying remanent magnetization effects in magnetic data. Geophysics. https://doi.org/10.1190/1.1443449
Rollinson H (2005) Chromite in the mantle section of the Oman ophiolite: a new genetic model. Island Arc. https://doi.org/10.1111/j.1440-1738.2005.00482.x
Shroder JF, Eqrar N, Waizy H, Ahmadi H, Weihs BJ (2022) Review of the geology of Afghanistan and its water resources. Int Geol Rev. https://doi.org/10.1080/00206814.2021.1904297
Sigmund Hammer L, Nettleton L, Hastings WK (1945) Gravimeter prospecting for chromite in Cuba. Geophysics. https://doi.org/10.1190/1.1437146
Sun J, Melo AT, Kim JD, Wei X (2020) Unveiling the 3D undercover structure of a Precambrian intrusive complex by integrating airborne magnetic and gravity gradient data into 3D quasi-geology model building. Interpretation. https://doi.org/10.1190/INT-2019-0273.1
Trevino SF, Miller CA, Tikoff B, Fournier D, Singer BS (2021) Multiple, coeval silicic magma storage domains beneath the laguna del maule volcanic field inferred from gravity investigations. J Geophys Res Solid Earth. https://doi.org/10.1029/2020JB020850
Xi X, Yang H, He L, Chen R (2013) Chromite mapping using induced polarization method based on spread spectrum technology. In: 26th symposium on the application of geophysics to engineering and environmental problems 2013, SAGEEP 2013. https://doi.org/10.4133/sageep2013-015.1
Yüngül S (1956) Prospecting for chromite with gravimeter and magnetometer over rugged topography in East Turkey. Geophysics. https://doi.org/10.1190/1.1438245

Publisher's Note